

The Compressional Beta Effect and Convective System Propagation[©]

HING ONG^a AND DA YANG^{a,b}

^a University of California, Davis, Davis, California

^b Lawrence Berkeley National Laboratory, Berkeley, California

(Manuscript received 9 August 2021, in final form 8 April 2022)

ABSTRACT: The compressional beta effect (CBE) arises in a compressible atmosphere with the nontraditional Coriolis terms (NCTs), the Coriolis force from the locally horizontal part of the planetary rotation. Previous studies proposed that the CBE speeds up the eastward propagation and slows down the westward propagation of zonal vertical circulations in a dry atmosphere. Here, we examine how the CBE affects the propagation of convectively coupled tropical waves. We perform 2D (x, z), large-domain cloud-resolving simulations with and without NCTs. This model setup mimics the atmosphere along Earth's equator, and differences between the simulations highlight the role of the CBE. We analyze precipitation, precipitable water, and surface and upper-level winds from our simulations. Gravity wave signals emerge in all fields. In the no-NCT simulation, eastward and westward gravity waves propagate at the same speed. With NCTs, eastward gravity waves propagate faster than westward gravity waves. To quantify the strength of the CBE, we then measure the difference in gravity wave speed and find that it linearly increases with the system rotation rate. This result is consistent with our theoretical prediction and suggests that the CBE can induce zonal asymmetry in propagation behaviors of convectively coupled waves.

SIGNIFICANCE STATEMENT: The rotation of Earth turns eastward motion upward and upward motion westward, and vice versa. This effect is called the nontraditional Coriolis effect and is omitted in most of the current atmospheric models for predicting weather and climate. Using an idealized model with cloud physics, this study suggests that the inclusion of the nontraditional Coriolis effect speeds up eastward-moving rainy systems and slows down westward-moving ones. The speed change agrees with a theory without cloud physics. This study encourages restoring the nontraditional Coriolis effect to the atmospheric models since it increases the accuracy of tropical large-scale weather prediction while the cost is low.

KEYWORDS: Tropics; Dynamics; Gravity waves; Madden-Julian oscillation; Atmospheric waves; Spectral analysis/models/distribution; Cloud resolving models; Idealized models

1. Introduction

Most global weather and climate models solve the primitive equations for Earth's atmosphere, assuming a thin atmosphere in the hydrostatic balance. To conserve energy and angular momentum, these models neglect the locally horizontal component of Earth's rotation vector. This is called the traditional approximation (Eckart 1960), and the neglected Coriolis components are known as the nontraditional Coriolis terms (NCTs; which are terms involving $2\Omega \cos\vartheta$, where Ω and ϑ denote planetary rotation rate and latitude). These approximations were believed to hold accurately for large-scale circulations in Earth's atmosphere (e.g., Vallis 2017).

However, recent studies have emphasized that NCTs can significantly affect thermodynamic states and atmospheric circulations in the tropics (Hayashi and Itoh 2012; Igel and Biello 2020; Ong and Roundy 2019, 2020a,b). For example, NCTs affect thickness between pressure levels—a measure of effective atmospheric buoyancy—by about 10% of the thickness variability (Ong and Roundy 2020a). Ong and Roundy

(2019) found that, in response to steady heat sources, NCTs can generate anomalous winds that are about 12% of the total wind response. Ong and Roundy (2020b, hereafter OR20b) further showed that NCTs produce an eastward propagation tendency for atmospheric waves in Earth's tropics. Ruling out other effects of NCTs by testing linear models, OR20b identified that the underlying mechanism was the compressional beta effect (CBE), which had been only considered significant in the atmosphere of giant planets and stars (e.g., Gilman and Glatzmaier 1981; Glatzmaier et al. 2009; Verhoeven and Stellmach 2014).

While the thickness theory (Ong and Roundy 2020a) is inherent to all the above-mentioned theories about NCTs, the CBE theory (OR20b) is dynamically distinct from the others by vorticity thinking. In the three-dimensional (3D) vorticity equation with the anelastic approximation on an equatorial beta plane (see appendix A for derivations), NCTs (2Ω given $\vartheta = 0$) appear in two terms:

$$\begin{aligned} \frac{\partial \boldsymbol{\omega}}{\partial t} + & \left[(\mathbf{v} \cdot \nabla) \boldsymbol{\omega} + \beta \mathbf{k} \times (\boldsymbol{\omega} \cdot \nabla) \mathbf{v} - \beta y \frac{\partial \mathbf{v}}{\partial z} \right. \\ & \left. + \beta y \frac{w}{H} \mathbf{k} - \nabla \times b \mathbf{k} \right] = 2\Omega \frac{\partial \mathbf{v}}{\partial y} - 2\Omega \frac{w}{H} \mathbf{j}. \end{aligned} \quad (1)$$

The variables are defined as follows: $\boldsymbol{\omega}$ is the 3D relative vorticity, \mathbf{v} is the 3D velocity, w is the vertical velocity, H is the

[©] Supplemental information related to this paper is available at the Journals Online website: <https://doi.org/10.1175/JAS-D-21-0219.s1>.

Corresponding author: Hing Ong, hxong@ucdavis.edu

scale height, v is meridional velocity, β is the meridional derivative of the traditional Coriolis parameter, and b is the buoyancy. The left-hand side shows terms without NCTs, including local tendency of vorticity and others (bracketed). The right-hand side shows terms with NCTs, including the stretching–tilting term (stretching of and tilting from meridional planetary vorticity) and the CBE term. The stretching–tilting term needs the meridional dimension while the CBE does not. The stretching–tilting term has been associated with zonal wind response to heat sources (Hayashi and Itoh 2012; Igel and Biello 2020; Ong and Roundy 2019).

These recent studies have advanced our understanding of NCTs. However, most of them were based on simple models with imposed flow field or prescribed moist physics and solved linear problems. Though Igel and Biello (2020) presented nonlinear cloud-resolving model (CRM) simulations, they focused on the stretching–tilting effect in our Eq. (1) (“Coriolis shear” in their words), which is distinct from the CBE. The present study uses a zonal vertical two-dimensional (2D) CRM to further explore possible effects of the CBE on explicitly simulated convectively coupled circulations. We remove the stretching–tilting effect by using the 2D domain. The 2D CRM experiments simulate gravity waves and self-aggregated convection (e.g., Held et al. 1993; Yang 2018) in radiative–convective equilibrium (RCE), and their propagation characteristics are examined given NCTs switched on and off.

The rest of this paper is organized as follows. Section 2 reviews the CBE and forms a hypothesis. Section 3 describes the methods of modeling and spectral analyses. Section 4 presents the results and tests the hypothesis. Section 5 summarizes this paper and discusses the implications for the Madden–Julian oscillation (MJO).

2. The CBE

OR20b introduced both NCTs and the vertically decreasing density to the wave theory on an equatorial beta plane (Matsuno 1966). The present study confines the domain to a zonal vertical plane at the equator. This choice of domain removes the traditional beta effect, which is the major source of west–east asymmetry of the inertio-gravity wave mode, isolating the CBE. Modified by the CBE, the dispersion relation of gravity waves can be approximated to the first order as follows. Start from rearranging Eq. (11) of OR20b and taking the quasi-hydrostatic approximation (see appendix A for details):

$$c^2 - \frac{2\Omega}{m_H^2 H} c - \frac{\tilde{N}^2}{m_H^2} = 0, \quad (2)$$

where the variables are defined as follows: c is the phase speed, \tilde{N} is the effective buoyancy frequency, and $m_H^2 \equiv m^2 + 1/(4H^2)$, where m denotes vertical wavenumber. Solve Eq. (2) for c :

$$c = \frac{\Omega}{m_H^2 H} \pm \frac{\tilde{N}}{m_H} \sqrt{1 + \left(\frac{\Omega}{m_H^2 H} \frac{m_H}{\tilde{N}} \right)^2}. \quad (3)$$

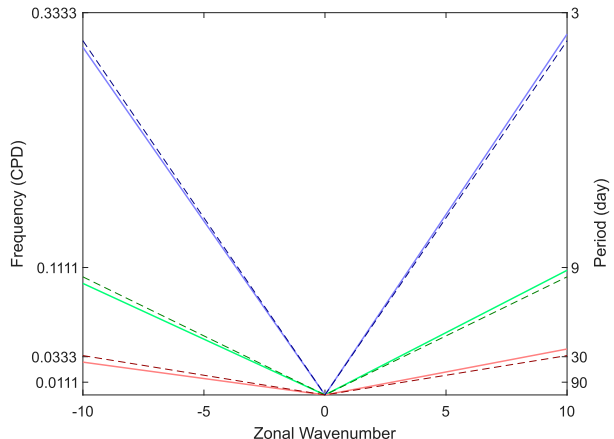


FIG. 1. Zonal temporal dispersion relations of gravity waves confined to a zonal vertical plane at the equator with the FOCBE parameter of Earth’s tropical troposphere of 0.265 m s^{-1} (solid) and without the FOCBE (dash). The red, green, and blue lines correspond to $\hat{\Omega}$ of $1/6$, $1/18$, and $1/54$, respectively.

Define $c_0 \equiv c(\Omega = 0) = \pm \tilde{N}/m_H$ and rewrite Eq. (3):

$$c = \frac{\Omega}{m_H^2 H} + c_0 \sqrt{1 + \left(\frac{\Omega}{m_H^2 H c_0} \right)^2}. \quad (4)$$

Using $\hat{c} \equiv c/c_0$ and $\hat{\Omega} \equiv \Omega/(m_H^2 H c_0)$, nondimensionalize Eq. (4):

$$\hat{c} = \hat{\Omega} + \sqrt{1 + \hat{\Omega}^2}. \quad (5)$$

Expand the square root in Eq. (5) around $\hat{\Omega}^2 = 0$:

$$\hat{c} = 1 + \hat{\Omega} + \frac{\hat{\Omega}^2}{2} + O(\hat{\Omega}^4). \quad (6)$$

Define $\Delta c \equiv c - c_0$ and dimensionalize Eq. (6):

$$\Delta c = \frac{\Omega}{m_H^2 H} + \frac{1}{2c_0} \left(\frac{\Omega}{m_H^2 H} \right)^2 + c_0 O(\hat{\Omega}^4). \quad (7)$$

The first term on the right-hand side is defined as the first-order CBE (FOCBE) parameter. A negative phase speed denotes westward propagation, and vice versa. Figure 1 depicts three pairs of c and c_0 in a wavenumber–frequency domain given the FOCBE parameter in the tropical troposphere derived from an observational dataset (see section 4 for estimation), and it shows that the FOCBE makes gravity waves propagate faster eastward and slower westward in a way that the dispersion lines rotate counterclockwise in the wavenumber–frequency domain. The higher-order terms are negligible since $\hat{\Omega}$ is small in general; for example, the three pairs of c_0 in Fig. 1 correspond to $\hat{\Omega}$ of $1/6$, $1/18$, and $1/54$ (from slow to fast). To our hypothesis, regarding a wavenumber in the whole space–time spectrum of simulated precipitation or other variables, the CBE may shift eastward power to a higher frequency and westward power to a lower frequency. Thus, the corresponding power shift

is counterclockwise. For gravity wave bands, the speed change is predicted by Eq. (7).

3. Methods

a. Model description

This study uses the System for Atmospheric Modeling (SAM) (Khairoutdinov and Randall 2003) version 6.11.2 and complies with the protocol of RCE Model Intercomparison Project (RCEMIP; Wing et al. 2018, 2020). We restored NCTs to SAM as released in version 6.11.7. The implementation of NCTs was validated by the compressional Rossby wave benchmark (OR20b). It increased the central processing unit (CPU) time by less than 0.01% of the total cost of full-physics simulations. The whole process from restoration, validation, to releasing was simple. Thus, the cost for NCTs was low. This is consistent with Skamarock et al. (2021), who reported that the restoration of NCTs increased the cost of the global atmospheric dynamical core by less than 5%. For spherical coordinates, a little extra care is needed to retain the angular momentum conservation (e.g., White and Bromley 1995). Since SAM uses Cartesian coordinates, the restoration is straightforward.

Deviations from the RCEMIP protocol (Wing et al. 2018) are explained as follows. First, six simulations are conducted with the system rotation rate set to 0, 1, 4, 8, 16, and 64 times Earth's rotation rate (named X00, X01, X04, X08, X16, and X64). Second, the meridional dimension is eliminated (2D). Third, the size of the zonal and temporal dimensions is 24 576 km and 1632 Earth's days. Fourth, the model top is lowered from 33 to 28 km. Last, mean zonal velocity is nudged toward zero by linear relaxation at a time scale of 86 400 s at each level to prevent development of mean winds that may affect convective system propagation.

All other procedures and settings follow the elongated channel SAM simulation over sea surface temperature of 300 K in RCEMIP (labeled SAM_CRM/RCE_large300). The initial vertical profile is derived from the corresponding small domain simulation data in RCEMIP (labeled SAM_CRM/RCE_small300). In theory, the X00 spectrum should be west–east symmetric.

b. Spectral analyses

To analyze the overall propagation characteristics of convective systems in the 2D RCE simulations, the data except the first 96 days are transformed into space–time spectra following the sampling procedure by Wheeler and Kiladis (1999, hereafter WK99) based on the method by Hayashi (1971, 1982). The sample length is 64 days. This procedure yields raw spectral power in the wavenumber–frequency domain. To focus on the east–west asymmetry, we contrast the raw spectra to reference spectra made from the X00 spectra by taking the average of spectral power density symmetric about wavenumber zero. We symmetrize the reference for two reasons. First, the X00 simulation does not distinguish west from east, so zonally flipped X00 spectra are equally valid as the

raw X00 spectra. Second, a symmetric reference spectrum would help highlight NCT-induced zonal asymmetry.

To measure the gravity wave speed, we take the power-weighted average of phase speed in a gravity wave band. Using the normalization procedure by WK99, we take contiguous bands with normalized power greater than unity following gravity wave dispersion lines as gravity wave bands. To quantify the uncertainty, we test the sample lengths of 128, 192, 256, 384, 512, and 768 days, and the smoothing passes in wavenumber of 16, 32, 48, and 64 times. The smoothing passes in frequency are set to the sample length divided by 8.

To estimate the vertical wavenumber relevant to the FOCBE parameter, the data are transformed into vertical normal modes assuming a rigid tropopause (Fulton and Schubert 1985) with the approximated set of analytic basis functions omitting small vertical variations of scale height and static stability (Kiladis et al. 2009) as follows:

$$\sqrt{\rho(z)}u(x, z, t) = \sum_{M=0}^{\infty} U_M(x, t) \cos\left(\frac{M\pi z}{D}\right), \quad z \in [0, D], \quad (8)$$

where the variables are defined as follows: ρ is the density, u is the zonal velocity, D is the tropopause height, and U_M is the amplitude of the M th vertical mode. The vertical wavenumber m equals to $M\pi/D$. The power U_M^2 is proportional to the vertically integrated kinetic energy of the vertical mode. Given the level of the minimum temperature in the mean profile, D is located at 15.5 km. The data are linearly interpolated to vertical levels equally spaced by $\Delta z = 500$ m from $\Delta z/2$ to $D - \Delta z/2$, and then $\sqrt{\rho}u$ is calculated. Then, the domain is extended to $2D - \Delta z/2$, and the upper half of the new domain is filled with the mirror image of $\sqrt{\rho}u$ from the lower half. For each profile, a fast Fourier transform is performed. The resulting coefficients can be filtered for a target time scale with the Lanczos filter. This procedure yields the vertical-mode spectrum.

For comparison, the same vertical-mode analysis is applied to an observational dataset. The dataset used is the Merged Sounding (Giangrande et al. 2011) over Gan Island, Maldives, from 1 October 2011 to 9 February 2012 during the Dynamics of the MJO (DYNAMO) field campaign (Yoneyama et al. 2013). The above-mentioned procedure is followed, but D and Δz are 17.0 km and 200 m.

4. Results

We first focus on the raw spectra without NCTs (top row of Fig. 2) of precipitation rate, precipitable water (PW), zonal velocity at the lowest level (USFC) and at 200 hPa (U200). They all show power peaks that follow the dispersion lines for convectively coupled gravity waves with a speed of about ± 16 m s $^{-1}$ (26-m equivalent depth). In addition, they show weaker peaks corresponding to dry gravity waves with a speed of about ± 42 m s $^{-1}$ (180-m equivalent depth) except in the precipitation spectrum (Fig. 2a). Here we take the power-weighted average of speed in each gravity wave band in the normalized U200 spectra (Figs. 3d,h,l). Moreover, the raw spectra (Fig. 2) show another pair of local power maxima

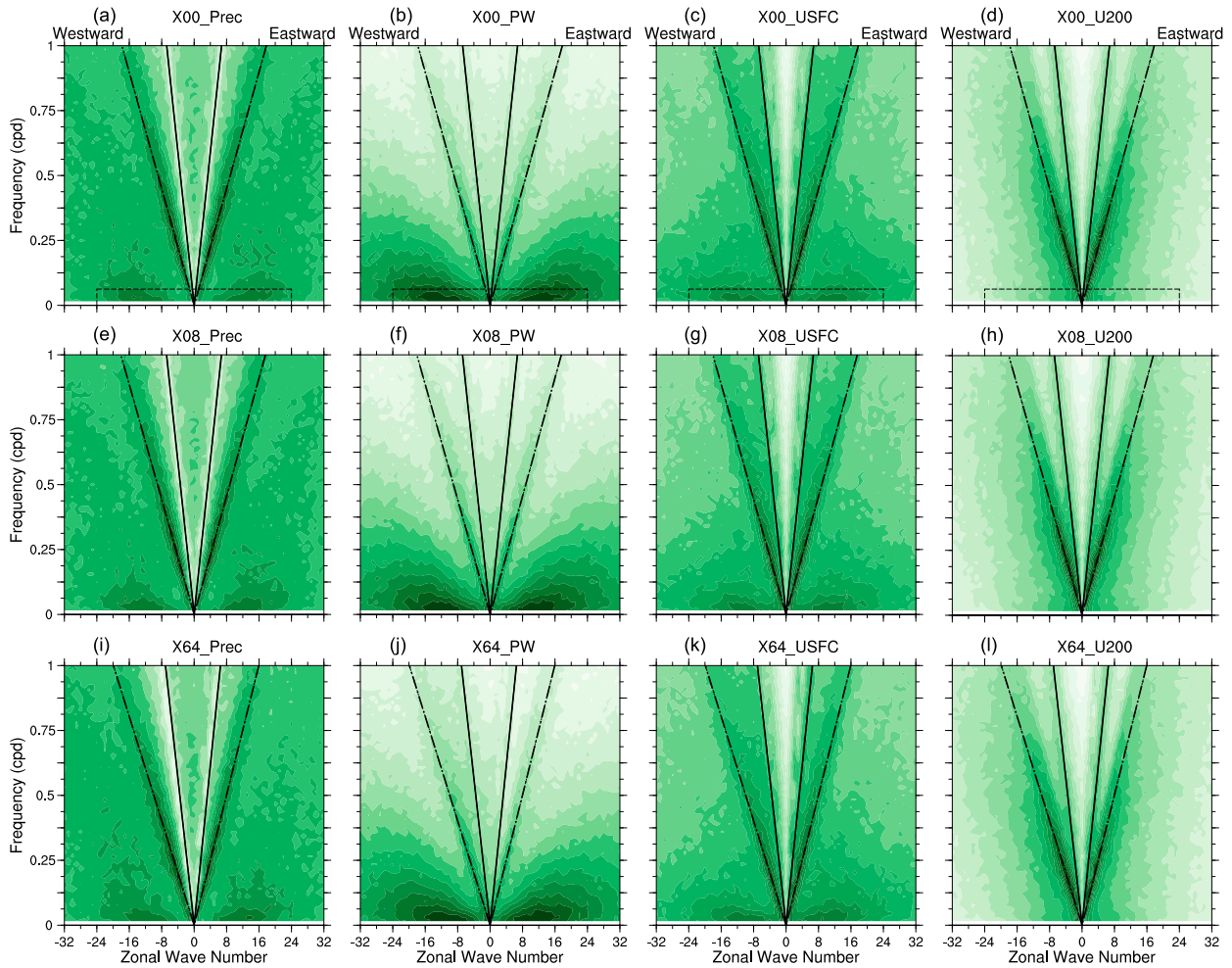


FIG. 2. Raw spectra of (from left to right) the precipitation rate, precipitable water, and zonal velocity at the lowest level and at 200 hPa, respectively, from (from top to bottom) the X00, X08, and X64 simulations, respectively. The darker shading denotes the larger base-10 logarithm of the power; the shading interval is 0.3 arbitrary units. The dashed and solid lines denote 26- and 180-m equivalent depths.

at the lowest resolved frequency at around wavenumber ± 12 except in the U200 spectra (Figs. 2d,h,l). These low-frequency spectral peaks correspond to slowly propagating long-lived convective systems with a characteristic wavelength of 2048 km, which conforms to the scale of the self-aggregated convective clusters in Yang's (2018) 2D RCE simulation over 300 K. Appendix B shows the evolution of the self-aggregated convection filtered for its band within the dashed box in the top row of Fig. 2. With increasing system rotation rate (from top to bottom of Fig. 2), the spectra seem similar, but the gravity wave peaks shift with the dispersion lines (both dashed and solid) significantly in the X64 spectra (bottom row of Fig. 2).

We compare Fig. 2 with the raw observed power spectra of eastward propagating convection symmetric about the equator (Fig. 1 of Roundy 2020; see also Kiladis et al. 2009; WK99). When convectively coupled, the simulated gravity waves (dashed lines in Fig. 2) as well as the observed Kelvin waves (e.g., Fig. 4b of WK99) correspond to an equivalent

depth of about 25 m. However, unlike the raw simulation spectra with multiple maxima in frequency (Fig. 2), the raw observational spectra do not show a peak in the Kelvin wave band. Instead, the Kelvin wave maximum emerges from the normalization by a smoothed background spectrum (Roundy 2020). Another notable difference lies in the horizontal scale of the low-frequency power maxima; the simulated convective clusters scale ~ 2000 km while the MJO scales $\sim 20\,000$ km.

To test our hypothesis of counterclockwise power shift in the wavenumber–frequency domain, we first contrast the X64 spectra to the symmetrized X00 spectra (bottom row of Fig. 4; section 3b). First, the precipitation spectrum (Fig. 2a) shows bands where the power decreases toward a higher frequency eastward or a lower frequency westward, including the counterclockwise side of the dashed lines, the clockwise side of the solid lines, and a band roughly covering wavenumbers from 4 to 12 and a frequency of 0.125 cycle per day (cpd) or lower. In these bands, the spectral power increases in the X64

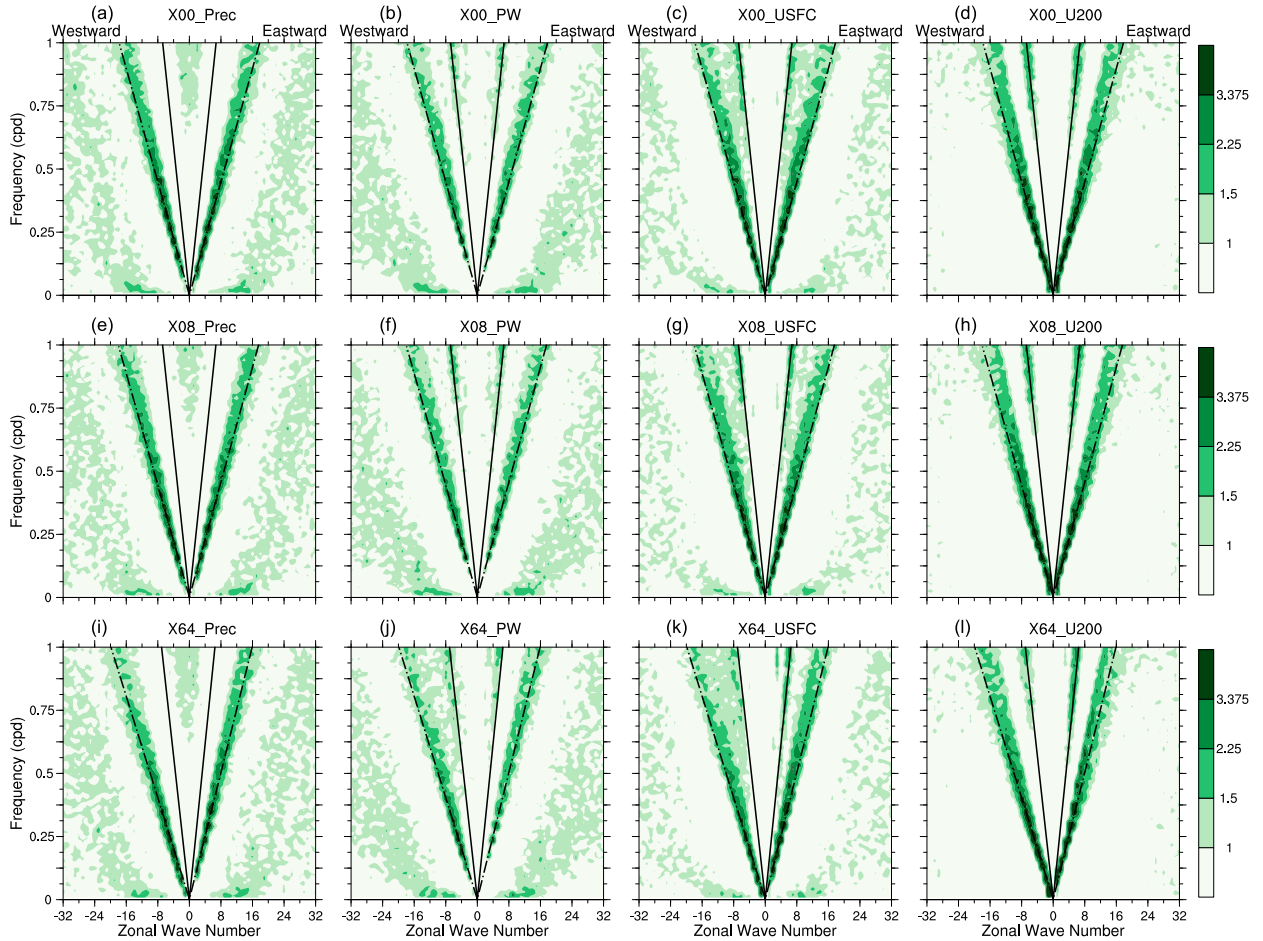


FIG. 3. As in Fig. 2, but depicting the ratio of the raw spectrum to the background spectrum. The sample length is set to 128 days. Each background spectrum is created by smoothing for 64 times in wavenumber and is different from one another.

spectrum (Fig. 4i) as if the CBE shifts the power counter-clockwise. Even the power minima in the precipitation spectrum associated with dry gravity waves (solid lines in Fig. 2a) shift toward a higher frequency eastward and a lower frequency westward (Fig. 4i). Similarly, in the USFC spectrum (Fig. 2c), such counterclockwise power shift due to the CBE occurs in bands including the counterclockwise side of the dashed and solid lines as well as a part of the self-aggregated convection band roughly within wavenumbers 2 and 14 along with its extension toward the dashed line. The power also increases in these bands in the X64 spectrum (Fig. 4k). On the other hand, the power generally decreases in these spectra (Figs. 4i,k) in the clockwise side of power maxima and counterclockwise side of power minima. Similar reasoning applies to the PW (Fig. 4j) and U200 (Fig. 4l) spectra except the upward side of the dispersion lines in the PW spectrum, which implies power changes in a nonshifting manner. With decreasing system rotation rate (from bottom to top of Fig. 4), the power ratio becomes noisy, but the above-mentioned power changes can mostly be found to have smaller magnitude.

To quantitatively test the FOCBE theory, we first estimate the FOCBE parameter. The simulations and the observations

yield different vertical-mode spectra of kinetic energy; the former peak at the third mode, but the latter peak at the first mode (Fig. 5). Unlike the observational red spectrum with a concentrated single maximum, the simulation spectra are characterized by not only the prominent third-mode peak but also weaker redness with energy dispersed into higher vertical modes (Fig. 5). Besides, the power slightly moves from the first two modes to higher when filtered for the time scale of simulated gravity waves (1.5–18 days in Fig. 2) and observed Kelvin waves (2.5–30 days in WK99). With these caveats, the most energetic vertical mode is taken to estimate the characteristic FOCBE parameter of the observation and each simulation (Table 1). The prominence of the third vertical mode in our simulations can lead to severe underestimation of the effect of NCTs according to the FOCBE theory; the theoretical gravity wave speed change is one-ninth of the first mode. Consequently, the X08 simulation best corresponds to Earth's tropical troposphere, where the first vertical mode seems to dominate. Also shown in Table 1, we use the speed of a convectively coupled gravity wave ($c_0 = 16 \text{ m s}^{-1}$) as the reference to nondimensionalize the FOCBE parameter [$\hat{\Omega} \equiv \Omega/(m_H^2 H c_0)$, see section 2]. The results suggest that the

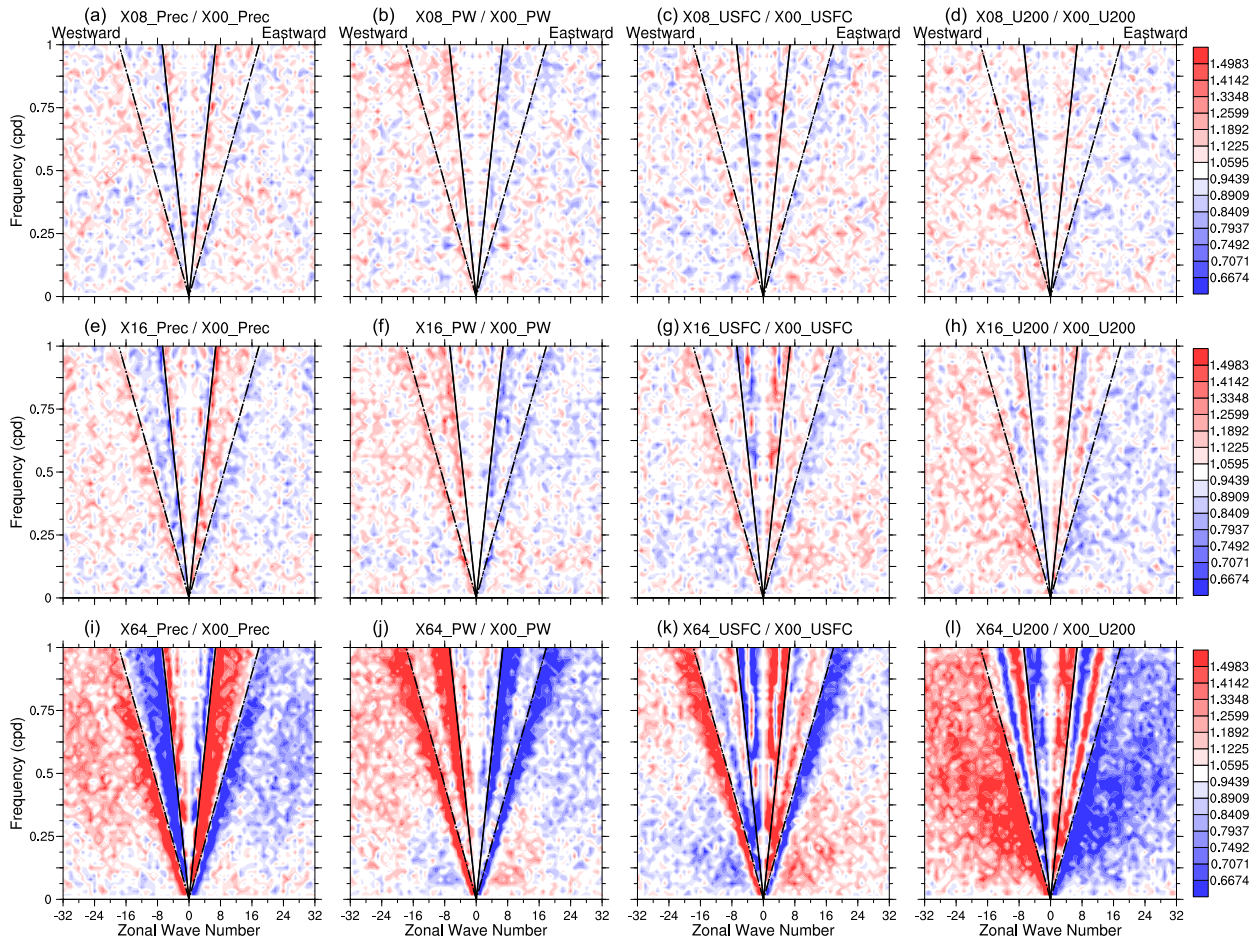


FIG. 4. As in Fig. 2, but the shading denotes the power ratio of the X08, X16, and X64 to the symmetrized X00. The shading levels are spaced by a common ratio of $\sqrt[12]{2}$ except that the level 1 is omitted.

CBE is insignificant with respect to the gravity wave. However, given c_0 in the denominator of $\hat{\Omega}$, slower-propagating phenomena could be more prone to the CBE.

The X08 spectra show power changes in frequency lower than the convectively coupled gravity wave bands (top row of Fig. 4). In the low-frequency USFC spectrum (Fig. 4c), the power increases in the eastward band and decreases in the westward band. However, in the U200 spectrum (Fig. 4d), the power changes are the opposite. To explain this contrast, we compare their low-frequency raw spectra (Figs. 2c,d). The USFC spectrum (Fig. 2c) is red mostly in frequency. Hence, taking a constant wavenumber, the counterclockwise power shift would lead to an eastward power increase and a westward power decrease. Similar explanations can be applied to parts of the precipitation and PW spectra (Figs. 4a,b). On the other hand, the U200 spectrum (Fig. 2d) is red mostly in wavenumber. Hence, taking a constant frequency, the shift would result in an eastward power decrease and a westward power increase. Though noisy in X08, these features are robust; they incrementally amplify in X16 and X64 results.

Finally, we test the FOCBE theory quantitatively. To avoid complication due to the proximity of the two types of gravity

wave peaks, here we measure the gravity wave speed from the normalized precipitation spectra (Fig. 3a column), where the dry gravity wave peaks are absent. The measured gravity wave speed (solid lines) captures the gravity wave peaks in the normalized spectra of the other variables (Fig. 3). As a caveat, the smoothed background spectra for the normalization also change with the system rotation rate. Nevertheless, our conclusion holds even when measuring the gravity wave speed from the raw spectra. We take the average of the positive and negative phase speed as the speed change (Δc).

The Δc results (Fig. 6) agree with their FOCBE parameter (Table 1). The X00 results are about zero and not shown in Fig. 6 because they include negative values, which cannot be converted to log scale. As shown in Fig. 6, the X01 results are almost undetectable because the asymmetry hardly stands out from the noise (see online supplemental material). The other simulation results are incremental to c (about 16 m s^{-1}) and discernible only by computers except that the X64 results yield Δc scaling 11% of c , which is noticeable by sight (bottom row of Figs. 2–4). Nevertheless, the robust agreement shown in Fig. 6 confirms that the dry-dynamical FOCBE theory can predict Δc due to the

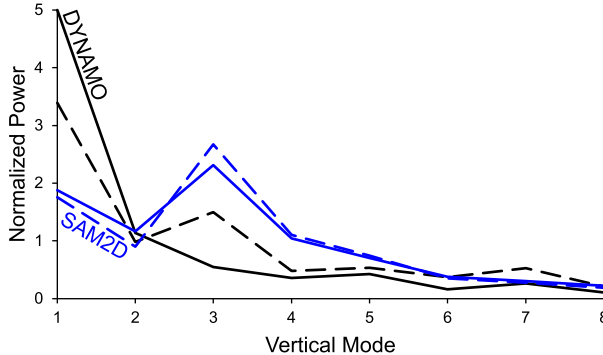


FIG. 5. Vertical-mode spectra of kinetic energy (power) derived from zonal velocity profiles in the Merged Sounding during DYNAMO (black) and the 2D RCE with SAM (blue), each unfiltered (solid) and filtered for the time scale of Kelvin or gravity waves (dashed; see text). The power is normalized by the average in the first eight modes.

inclusion of NCTs even given the free interactions between circulation and moist physics in the 2D RCE.

5. Summary and discussion

This study explores one of the effects of the nontraditional Coriolis terms (NCTs), specifically the compressional beta effect (CBE), on explicitly simulated convective system propagation in radiative-convective equilibrium (RCE) in a zonal vertical domain using the System for Atmospheric Modeling (SAM). The use of a zonal vertical domain eliminates the other effect of NCTs, the stretching-tilting effect. We restored NCTs to SAM to represent the effects of system rotation about a meridional axis. The system rotation rate is tested over a wide range. We hypothesize that the CBE makes the eastward propagation of convectively coupled circulations faster and the westward propagation slower. The simulated propagation characteristics are analyzed with space-time spectra. The raw spectra show local power maxima in bands associated with self-aggregated convection and convectively coupled gravity waves. Given the power spectra red in frequency, the CBE can qualitatively explain the power increase in the band of eastward propagating convective clusters and its decrease in the band of westward ones. Furthermore, this study measures the speed change of convectively coupled gravity waves from the precipitation spectra. The resulting speed change agrees with the theoretical speed change due to the FOCBE, which is estimated from the system rotation rate, the scale height, and the vertical wavenumber derived from the vertical-mode analysis. In this idealized framework, these changes due to the inclusion of NCTs are robust and meaningful while the computational cost for the implementation of NCTs in SAM increases by less than 0.01%. Also given that the restoration of NCTs to the dynamical core is simple, we recommend it for model development.

These results, for the first time, show that NCTs can affect convective system propagation because of the CBE, which was derived from dry dynamics. The dry-dynamical theory agrees

TABLE 1. The characteristic FOCBE parameter.

Case name	Ω^a	M	D (km)	H (km) ^b	FOCBE (m s ⁻¹)	$\hat{\Omega}$ (%) ^c
DYNAMO	1	1	17.0	7.0	0.265	1.66
X00	0	3	15.5	7.0	0	0
X01	1	3	15.5	7.0	0.028	0.17
X04	4	3	15.5	7.0	0.111	0.69
X08	8	3	15.5	7.0	0.222	1.39
X16	16	3	15.5	7.0	0.445	2.78
X64	64	3	15.5	7.0	1.779	11.12

^a Normalized by Earth's rotation rate of $7.292 \times 10^{-5} \text{ s}^{-1}$.

^b Virtual temperature times gas constant divided by gravity acceleration averaged in the troposphere with the data equally spaced in height.

^c FOCBE divided by a convectively coupled gravity wave speed of 16 m s^{-1} .

with the moist simulation results over a wide range of the FOCBE parameter (Fig. 6). Such agreement allows us to infer changes in convective system propagation from the FOCBE parameter. Among our simulations, the one with an 8-times Earth's rotation rate may be comparable to Earth's tropical troposphere, because the first vertical mode dominates in the observations while the third mode is the strongest in our simulations.

The use of a zonal vertical 2D domain simplifies the interpretation of the results but limits their applicability to the real tropical atmosphere. The 2D domain disables the stretching and tilting of vorticity, leaving the CBE the only way for

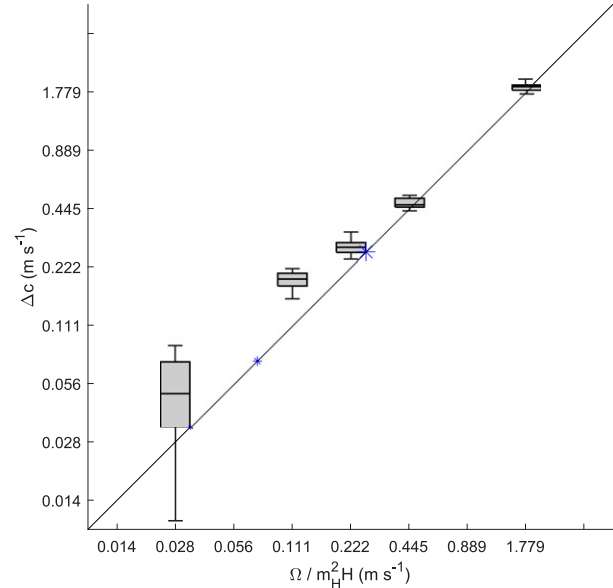


FIG. 6. Scaling of the gravity wave speed change (boxes and whiskers) against the FOCBE parameter (horizontal axis; see Table 1). Each box-and-whiskers set denotes the quartiles and full range of the speed measurement results from each simulation. The blue star marks denote the first, second, and third vertical modes (from right to left) from the Merged Sounding during DYNAMO; the mark sizes are proportional to the unfiltered power. The axes are log scaled.

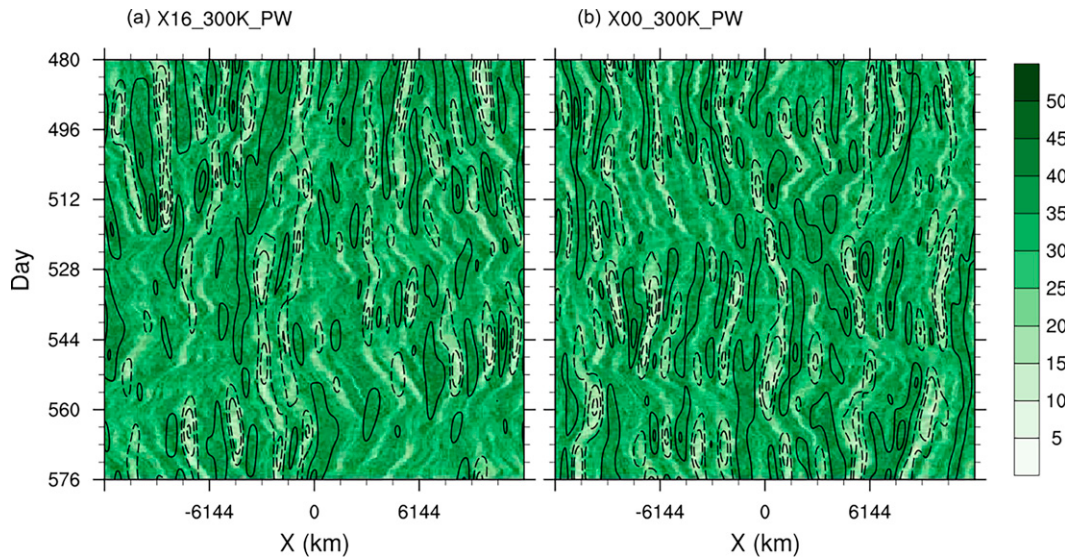


FIG. B1. Hovmöller diagrams of the PW in the 2D RCE (a) with NCTs (X16) and (b) without NCTs from the raw data (shading; mm) and data filtered for the self-aggregated convection (contours; interval: 5 mm). The solid and dashed contours denote positive and negative values, respectively, and the zero contour is omitted.

NCTs to affect the vorticity dynamics. However, the 2D domain also disables the traditional beta effect, which is the major source of west–east asymmetry of real equatorial waves. To better assess the relevance of NCTs in the real tropical atmosphere, further tests with general circulation models are needed. Though OR20b showed that NCTs cannot affect atmospheric wave propagation by the stretching–tilting effect in linear models, neither OR20b nor the present study can rule out this effect from affecting convective system propagation through 3D nonlinear processes.

For Earth's tropical troposphere, the FOCBE theory implies a gravity wave speed change of one FOCBE parameter, 0.265 m s^{-1} , which scales only 2% of the gravity wave speed itself. Yet this change may have implications for the propagation speed of the MJO. Regarding the MJO speed, the FOCBE can be introduced to two of the diverse MJO theories. First, Yang and Ingersoll (2013) determined the MJO speed by the average of inertio-gravity wave speed (negative westward and vice versa), which may increase by one FOCBE parameter. Second, Kim and Zhang (2021) proposed that the MJO speed arises from the damped Kelvin wave speed, which may speed up by one FOCBE parameter. However, given the diversity of MJO theories (Zhang et al. 2020), further studies are needed.

Our results show that the CBE can produce a significant east–west asymmetry in the spectral power density of precipitation, PW, and winds. Given a power spectrum red in frequency, NCTs can lead to enhanced power of low-frequency variability of eastward propagating signals (e.g., Figs. 4a–c), which are associated with convective self-aggregation in our simulations and might become the MJO in the real atmosphere. Therefore, restoring NCTs in atmospheric models may improve the representation of the MJO, the variability of

which is significantly underestimated by the current climate models (Le et al. 2021).

Acknowledgments. This research is supported by a Packard Fellowship awarded to D.Y. We thank Brandon Wolding and two anonymous reviewers for their useful comments.

Data availability statement. We thank the German Climate Computing Center (DKRZ) for hosting the standardized RCEMIP data, which are publicly available at <https://hdl.handle.net/21.14101/d4bee8e-6996-453e-bbd1-ff53b6874c0e>. The Merged Sounding data were obtained from the Atmospheric Radiation Measurement (ARM) Program sponsored by the U.S. Department of Energy, Office of Science, Office of Biological and Environmental Research, Climate and Environmental Sciences Division via doi:10.5439/1034922 with free registration. The model, SAM, can be used only with permission from Marat Kharoutdinov (marat.kharoutdinov@stonybrook.edu).

APPENDIX A

Derivations

To derive Eq. (1), start from the 3D momentum equation on an equatorial beta plane:

$$\frac{\partial \mathbf{v}}{\partial t} + (\mathbf{v} \cdot \nabla) \mathbf{v} + \beta y \mathbf{k} \times \mathbf{v} + \nabla \varphi - b \mathbf{k} = -2\Omega \mathbf{j} \times \mathbf{v},$$

where φ denotes the pressure-like variable defined by Lipps and Hemler (1982). Taking the curl and applying $\nabla \cdot \mathbf{v} = w/H$ (i.e., the anelastic approximation) yields Eq. (1).

To derive Eq. (2), first take the meridional component of Eq. (1), confine the domain to zonal and vertical, and linearize it around a motionless reference state:

$$\frac{\partial}{\partial t} \left(\frac{\partial u}{\partial z} - \epsilon \frac{\partial w}{\partial x} \right) + \frac{\partial b}{\partial x} + 2\Omega \frac{w}{H} = 0,$$

where ϵ serves to dynamically trace the vertical acceleration term during the derivation. Then, eliminate b by applying $\partial b / \partial t = -\tilde{N}^2 w$:

$$\frac{\partial^2}{\partial t^2} \left(\frac{\partial u}{\partial z} - \epsilon \frac{\partial w}{\partial x} \right) - \tilde{N}^2 \frac{\partial w}{\partial x} + \frac{2\Omega}{H} \frac{\partial w}{\partial t} = 0.$$

Next, rewrite the equation in terms of Ψ , where $\rho u = \partial \Psi / \partial z$ and $\rho w = -\partial \Psi / \partial x$:

$$\frac{\partial^2}{\partial t^2} \left(\epsilon \frac{\partial^2 \Psi}{\partial x^2} + \frac{\partial^2 \Psi}{\partial z^2} + \frac{1}{H} \frac{\partial \Psi}{\partial z} \right) + \tilde{N}^2 \frac{\partial^2 \Psi}{\partial x^2} - \frac{2\Omega}{H} \frac{\partial}{\partial t} \frac{\partial \Psi}{\partial x} = 0.$$

Last, assume plane wave solutions, $\Psi = \hat{\Psi} \exp(-z/2H) \exp[i(kx + mz - \omega t)]$, where k and ω denote wavenumber and frequency, and find the dispersion relation:

$$\left(\epsilon k^2 + m^2 + \frac{1}{4H^2} \right) \frac{\omega^2}{k^2} - \frac{2\Omega}{H} \frac{\omega}{k} - \tilde{N}^2 = 0.$$

This is equivalent to Eq. (11) of OR20b. Setting ϵ to zero (i.e., the quasi-hydrostatic approximation) and applying $c \equiv \omega/k$ yields Eq. (2).

APPENDIX B

Filtering for the Self-Aggregated Convection

To confirm the association of the self-aggregated convection with the spectral band in the dashed box in the top row of Fig. 2, the PW is filtered for this band. The Hovmöller diagrams of the filtered PW (Fig. B1) show many convective clusters (solid contours) and dry regions (dashed contours). These systems grow (or split), migrate, and decay (or merge) in a complex manner with generally 12 convective clusters maintained in total. Such metabolism occurs in periods other than the 96 days shown in Fig. B1.

REFERENCES

- Eckart, C., 1960: *Hydrodynamics of Oceans and Atmospheres*. Pergamon Press, 290 pp., <https://doi.org/10.1016/C2013-0-01648-9>.
- Fulton, S. R., and W. H. Schubert, 1985: Vertical normal mode transforms: Theory and application. *Mon. Wea. Rev.*, **113**, 647–658, [https://doi.org/10.1175/1520-0493\(1985\)113<0647:VNMTTA>2.0.CO;2](https://doi.org/10.1175/1520-0493(1985)113<0647:VNMTTA>2.0.CO;2).
- Giangrande, S., G. Mace, and D. Turner, 2011: Merged Sounding (MERGESONDE1MACE). ARM User Facility, accessed 4 April 2021, <https://doi.org/10.5439/1034922>.
- Gilman, P. A., and G. A. Glatzmaier, 1981: Compressible convection in a rotating spherical shell. I—Anelastic equations. II—A linear anelastic model. III—Analytic model for compressible vorticity waves. *Astrophys. J.*, **45** (Suppl.), 335–388.
- Glatzmaier, G. A., M. Evonuk, and T. M. Rogers, 2009: Differential rotation in giant planets maintained by density-stratified turbulent convection. *Geophys. Astrophys. Fluid Dyn.*, **103**, 31–51, <https://doi.org/10.1080/03091920802221245>.
- Hayashi, M., and H. Itoh, 2012: The importance of the nontraditional Coriolis terms in large-scale motions in the tropics forced by prescribed cumulus heating. *J. Atmos. Sci.*, **69**, 2699–2711, <https://doi.org/10.1175/JAS-D-11-0334.1>.
- Hayashi, Y., 1971: A generalized method of resolving disturbances into progressive and retrogressive waves by space Fourier and time cross-spectral analyses. *J. Meteor. Soc. Japan*, **49**, 125–128, https://doi.org/10.2151/jmsj1965.49.2_125.
- , 1982: Space-time spectral analysis and its applications to atmospheric waves. *J. Meteor. Soc. Japan*, **60**, 156–171, https://doi.org/10.2151/jmsj1965.60.1_156.
- Held, I. M., R. S. Hemler, and V. Ramaswamy, 1993: Radiative-convective equilibrium with explicit two-dimensional moist convection. *J. Atmos. Sci.*, **50**, 3909–3927, [https://doi.org/10.1175/1520-0469\(1993\)050<3909:RCEWET>2.0.CO;2](https://doi.org/10.1175/1520-0469(1993)050<3909:RCEWET>2.0.CO;2).
- Igel, M. R., and J. A. Biello, 2020: The nontraditional Coriolis terms and tropical convective clouds. *J. Atmos. Sci.*, **77**, 3985–3998, <https://doi.org/10.1175/JAS-D-20-0024.1>.
- Khairoutdinov, M. F., and D. A. Randall, 2003: Cloud resolving modeling of the ARM summer 1997 IOP: Model formulation, results, uncertainties, and sensitivities. *J. Atmos. Sci.*, **60**, 607–625, [https://doi.org/10.1175/1520-0469\(2003\)060<0607:CRMOTA>2.0.CO;2](https://doi.org/10.1175/1520-0469(2003)060<0607:CRMOTA>2.0.CO;2).
- Kiladis, G. N., M. C. Wheeler, P. T. Haertel, K. H. Straub, and P. E. Roundy, 2009: Convectively coupled equatorial waves. *Rev. Geophys.*, **47**, RG2003, <https://doi.org/10.1029/2008RG000266>.
- Kim, J.-E., and C. Zhang, 2021: Core dynamics of the MJO. *J. Atmos. Sci.*, **78**, 229–248, <https://doi.org/10.1175/JAS-D-20-0193.1>.
- Le, P. V., C. Guilloteau, A. Mamalakis, and E. Foufoula-Georgiou, 2021: Underestimated MJO variability in CMIP6 models. *Geophys. Res. Lett.*, **48**, e2020GL092244, <https://doi.org/10.1029/2020GL092244>.
- Lipps, F. B., and R. S. Hemler, 1982: A scale analysis of deep moist convection and some related numerical calculations. *J. Atmos. Sci.*, **39**, 2192–2210, [https://doi.org/10.1175/1520-0469\(1982\)039<2192:ASAODM>2.0.CO;2](https://doi.org/10.1175/1520-0469(1982)039<2192:ASAODM>2.0.CO;2).
- Matsuno, T., 1966: Quasi-geostrophic motions in the equatorial area. *J. Meteor. Soc. Japan*, **44**, 25–43, https://doi.org/10.2151/jmsj1965.44.1_25.
- Ong, H., and P. E. Roundy, 2019: Linear effects of nontraditional Coriolis terms on intertropical convergence zone forced large-scale flow. *Quart. J. Roy. Meteor. Soc.*, **145**, 2445–2453, <https://doi.org/10.1002/qj.3572>.
- , and —, 2020a: Nontraditional hypsometric equation. *Quart. J. Roy. Meteor. Soc.*, **146**, 700–706, <https://doi.org/10.1002/qj.3703>.
- , and —, 2020b: The compressional beta effect: Analytical solution, numerical benchmark, and data analysis. *J. Atmos. Sci.*, **77**, 3721–3732, <https://doi.org/10.1175/JAS-D-20-0124.1>.
- Roundy, P. E., 2020: Interpretation of the spectrum of eastward-moving tropical convective anomalies. *Quart. J. Roy. Meteor. Soc.*, **146**, 795–806, <https://doi.org/10.1002/qj.3709>.
- Skamarock, W. C., H. Ong, and J. B. Klemp, 2021: A fully compressible nonhydrostatic deep-atmosphere equations solver for

- MPAS. *Mon. Wea. Rev.*, **149**, 571–583, <https://doi.org/10.1175/MWR-D-20-0286.1>.
- Vallis, G. K., 2017: *Atmospheric and Oceanic Fluid Dynamics*. Cambridge University Press, 946 pp., <https://doi.org/10.1017/9781107588417>.
- Verhoeven, J., and S. Stellmach, 2014: The compressional beta effect: A source of zonal winds in planets? *Icarus*, **237**, 143–158, <https://doi.org/10.1016/j.icarus.2014.04.019>.
- Wheeler, M., and G. N. Kiladis, 1999: Convectively coupled equatorial waves: Analysis of clouds and temperature in the wavenumber-frequency domain. *J. Atmos. Sci.*, **56**, 374–399, [https://doi.org/10.1175/1520-0469\(1999\)056<0374:CCEWAO>2.0.CO;2](https://doi.org/10.1175/1520-0469(1999)056<0374:CCEWAO>2.0.CO;2).
- White, A. A., and R. Bromley, 1995: Dynamically consistent, quasi-hydrostatic equations for global models with a complete representation of the Coriolis force. *Quart. J. Roy. Meteor. Soc.*, **121**, 399–418, <https://doi.org/10.1002/qj.49712152208>.
- Wing, A. A., K. A. Reed, M. Satoh, B. Stevens, S. Bony, and T. Ohno, 2018: Radiative–Convective Equilibrium Model Intercomparison Project. *Geosci. Model Dev.*, **11**, 793–813, <https://doi.org/10.5194/gmd-11-793-2018>.
- , and Coauthors, 2020: Clouds and convective self-aggregation in a multimodel ensemble of radiative-convective equilibrium simulations. *J. Adv. Model. Earth Syst.*, **12**, e2020MS002138, <https://doi.org/10.1029/2020MS002138>.
- Yang, D., 2018: Boundary layer height and buoyancy determine the horizontal scale of convective self-aggregation. *J. Atmos. Sci.*, **75**, 469–478, <https://doi.org/10.1175/JAS-D-17-0150.1>.
- , and A. P. Ingersoll, 2013: Triggered convection, gravity waves, and the MJO: A shallow-water model. *J. Atmos. Sci.*, **70**, 2476–2486, <https://doi.org/10.1175/JAS-D-12-0255.1>.
- Yoneyama, K., C. Zhang, and C. N. Long, 2013: Tracking pulses of the Madden–Julian oscillation. *Bull. Amer. Meteor. Soc.*, **94**, 1871–1891, <https://doi.org/10.1175/BAMS-D-12-00157.1>.
- Zhang, C., Á. Adames, B. Khouider, B. Wang, and D. Yang, 2020: Four theories of the Madden–Julian oscillation. *Rev. Geophys.*, **58**, e2019RG000685, <https://doi.org/10.1029/2019RG000685>.